

# GRINtrode: a neural implant for simultaneous two-photon imaging and extracellular electrophysiology in freely moving animals

Connor M. McCullough<sup>a</sup>,<sup>✉</sup> Daniel Ramirez-Gordillo,<sup>b</sup> Michael Hall,<sup>c</sup>  
Gregory L. Futia,<sup>a</sup> Andrew K. Moran,<sup>d</sup> Emily A. Gibson<sup>a,\*</sup>,<sup>✉</sup>,<sup>†</sup>  
and Diego Restrepo<sup>d,\*</sup>,<sup>†</sup>

<sup>a</sup>University of Colorado Anschutz Medical Campus, Department of Bioengineering,  
Aurora, Colorado, United States

<sup>b</sup>University of Colorado Anschutz Medical Campus, Department of Neurosurgery,  
Aurora, Colorado, United States

<sup>c</sup>University of Colorado Anschutz Medical Campus, Neuroscience Machine Shop,  
Aurora, Colorado, United States

<sup>d</sup>University of Colorado Anschutz Medical Campus, Department of Cell and Development  
Biology, Aurora, Colorado, United States

## Abstract

**Significance:** *In vivo* imaging and electrophysiology are powerful tools to explore neuronal function that each offer unique complementary information with advantages and limitations. Capturing both data types from the same neural population in the freely moving animal would allow researchers to take advantage of the capabilities of both modalities and further understand how they relate to each other.

**Aim:** Here, we present a head-mounted neural implant suitable for *in vivo* two-photon imaging of neuronal activity with simultaneous extracellular electrical recording in head-fixed or fiber-coupled freely moving animals.

**Approach:** A gradient refractive index (GRIN) lens-based head-mounted neural implant with extracellular electrical recording provided by tetrodes on the periphery of the GRIN lens was chronically implanted. The design of the neural implant allows for recording from head-fixed animals, as well as freely moving animals by coupling the imaging system to a coherent imaging fiber bundle.

**Results:** We demonstrate simultaneous two-photon imaging of GCaMP and extracellular electrophysiology of neural activity in awake head-fixed and freely moving mice. Using the collected information, we perform correlation analysis to reveal positive correlation between optical and local field potential recordings.

**Conclusion:** Simultaneously recording neural activity using both optical and electrical methods provides complementary information from each modality. Designs that can provide such bi-modal recording in freely moving animals allow for the investigation of neural activity underlying a broader range of behavioral paradigms.

© The Authors. Published by SPIE under a Creative Commons Attribution 4.0 International License. Distribution or reproduction of this work in whole or in part requires full attribution of the original publication, including its DOI. [DOI: [10.1117/1.NPh.9.4.045009](https://doi.org/10.1117/1.NPh.9.4.045009)]

**Keywords:** multiphoton imaging; freely moving; fiber imaging; electrophysiology; *in vivo*.

Paper 22041GR received May 30, 2022; accepted for publication Nov. 1, 2022; published online Dec. 1, 2022.

\*Address all correspondence to Emily A. Gibson, [emily.gibson@cuanschutz.edu](mailto:emily.gibson@cuanschutz.edu); Diego Restrepo, [diego.restrepo@cuanschutz.edu](mailto:diego.restrepo@cuanschutz.edu)

<sup>†</sup>Co-senior authors.

## 1 Introduction

*In vivo* recording of neural activity allows researchers to probe the function of neural circuits in action. The oldest method for this type of recording is electrophysiological recording of the extracellular field potential.<sup>1</sup> Implanted electrodes can record neural oscillations due to ensemble activity of large numbers of neurons known as local field potential (LFP), as well as spiking activity from single neurons when multiple recording sites are used.<sup>2-4</sup> Electrodes can be implanted to deep brain regions with limited damage to tissue and offer excellent temporal resolution with sampling rates in the tens of kilohertz capable of recording the changes in field potential elicited by action potential firing and synaptic activity. However, *in vivo* recording of LFPs has limitations in the ability to resolve single neuron activity. The recording field of an electrode is spatially limited by an inverse-square law limiting the number of neurons that can be sampled per electrode, and electrical recording does not provide high-resolution spatial information regarding the position of recorded cells relative to the recording site.

Optical techniques can overcome these spatial hurdles by allowing for *in vivo* neural recordings at single neuron resolution. These techniques use fluorescent dyes or genetically encoded indicators with fluorescence intensity that changes as a function of intracellular ionic concentration (typically calcium),<sup>5</sup> neurotransmitter release,<sup>6</sup> or membrane voltage.<sup>7,8</sup> Optical methods allow for recording from large numbers of neurons with known spatial localization allowing researchers to study spatial network dynamics and record from the same neurons longitudinally. Expression of these fluorescent reporters can be localized to specific cell types by genetically targeted expression. However, the temporal resolution of optical recordings is limited by the dynamics of the fluorescent reporter and acquisition rate of the microscope used, and fluorescent reporters based on ionic concentration are only a proxy of spiking. In addition, optical indicators do not provide the information on coordinated neuronal activity relevant to the flow of neural information<sup>9</sup> that is provided by LFP recordings.

Efforts have been made to combine optical and electrical recording modalities using transparent electrodes underlying a cranial window, but this limits the recording area to superficial structures.<sup>10</sup> The popular Miniscope<sup>11</sup> platform has also been used to achieve simultaneous optical and electrical recordings,<sup>12</sup> but this method is limited to one-photon imaging, and fabricating the device may prove difficult to labs without specialized microelectromechanical equipment for manufacturing the electrode array. More easily constructed single electrode-based designs have been developed,<sup>13</sup> but this method is restricted to head-fixed animals and faces limitations in isolating single units presented by single electrode recording modalities. Additional methods based on silicon probes have been developed,<sup>13</sup> which provide multisite recording, but present a complex multicomponent surgery and are limited to head-fixed mice.

Here, we describe the development of a low-cost gradient refractive index (GRIN) lens and tetrode-based device, which we name the GRINtrode. The GRINtrode allows for simultaneous two-photon imaging of neuronal activity using GCaMP (a synthetic fusion of green fluorescent protein, calmodulin, and M13, a peptide sequence from myosin light-chain kinase) fluorescent calcium indicators and extracellular field potential recorded from tetrodes surrounding a chronically implanted GRIN lens. The GRINtrode allows for multiphoton imaging and electrical recording in head-fixed animals, as well as in freely moving animals by coupling the imaging system to a coherent imaging fiber bundle. Tetrodes provide the advantage of multisite recording, allowing for isolation of single unit electrical activity. The GRINtrode also includes a ventral drive mechanism to advance the implant depth postsurgery. We provide examples of this dual recording and an analysis of the correlations between the fluorescent GCaMP activity traces and LFP or single unit electrical activity.

## 2 Materials and Methods

### 2.1 GRINtrode Design and Fabrication

The GRINtrode components were designed in SolidWorks three-dimensional CAD software (Dassault Systèmes). Aluminum GRINtrode bodies, polyetheretherketone (PEEK) drive thumb screws, Delrin rods, and vented 4-40 socket head cap screws were machined by the Neuroscience

Machine Shop at the University of Colorado Anschutz Medical Campus. Polyimide tubing was obtained from MicroLumen, Inc. GRIN lenses were obtained from GRINtech GmbH and Inscopix, Inc. Tetrodes are spun using a magnetic stirring plate<sup>14</sup> from 12.7- $\mu\text{m}$  diameter polyimide-coated nichrome wire (Sandvik, PX000001), bonded using a heat gun set to 235°C, and impedance is set to 250 to 500 k $\Omega$  by gold plating using a BAK Electronics IMP-2A and Neuralynx gold plating solution. Tetrodes are fixed around the periphery of the GRIN lens in a cross pattern using Loctite Ultra Gel cyanoacrylate glue (Loctite PN 1906107) and isolated from the imaging optic channel and vented screw using concentric sections of polyimide tubing. Tetrodes were cut by hand to extend  $\sim$ 200 to 300  $\mu\text{m}$  below the implanted GRIN lens surface to place the electrical recording sites close to the imaging plane of the GRIN lens system. Electrodes were pinned to a Neuralynx electrode interface board (EIB)-16 and then covered with 2-part epoxy (Gorilla Glue PN 4200101).

The GRINtrode utilizes a 9-mm GRIN relay lens, which is chronically implanted into the tissue with the device, referred to as the implanted GRIN lens. We have used both GRINtech 1-mm diameter  $\times$  9-mm length lenses (GRINtech NEM-100-25-10-860-S-1.0p) and Inscopix 1-mm diameter  $\times$  9-mm length lenses (Inscopix 1050-002177) for the implanted GRIN lens. Above the implanted GRIN lens is an empty polyimide tube, which creates a channel to allow for an additional imaging optic to be inserted [Fig. 1(a)]. The imaging optic channel is covered with Parafilm and sealed with Kwik-Sil silicone elastomer (World Precision Instruments, order code KWIL-SIL) between imaging sessions. For head-fixed imaging, the imaging optic is another GRIN lens, referred to as the imaging GRIN lens [Figs. 1(b) and 1(c)]. We have used either GRINtech 0.85-mm diameter  $\times$  10.8-mm length (NEM-085-45-10-860-S-1.5p) or GRINtech 1-mm diameter  $\times$  14.07-mm length (NEM-100-25-10-860-S-1.5p) GRIN lenses as the imaging GRIN lens.

For fiber coupled imaging, a coherent imaging fiber bundle was inserted into the imaging optic channel [Fig. 1(d)]. A 1.5-m-long Fujikura FIGH-15-600N coherent imaging fiber bundle was used for two-photon fiber-coupled imaging. For one-photon fiber-coupled imaging (Fig. S1 in the [Supplementary Material](#)), the coherent imaging fiber bundle was epoxied to a GRIN doublet lens, GRINtech 1-mm diameter  $\times$  8.09-mm length doublet GRIN lens (NEM-100-25-10-860-DS). The doublet GRIN lens introduces a 2.6 $\times$  magnification, which serves to demagnify the core-to-core spacing of the coherent imaging fiber bundle, improving the effective lateral resolution of the imaging system. However, using this additional GRIN doublet lens also restricts the field of view, and for two-photon fiber coupled imaging, there was a decrease in power throughput. The fiber-implanted GRIN spacing was adjusted using a Sutter Instruments MPC-325 micromanipulator, and the fiber was locked into place using a set screw.

## 2.2 Microscope Setup

A Sutter Instruments movable objective microscope was used to perform head-fixed *in vivo* 2P imaging through the GRINtrode. The excitation source was a Spectra-Physics MaiTai DeepSee HP Ti:Sapphire laser with  $\sim$ 80-fs pulses tuned to a center wavelength of 920 nm and operating at 80-MHz pulse repetition rate. Emission was collected through a 525/50 nm bandpass filter (Semrock PN FF03-525/50-25). For head-fixed recordings an Edmund Optics 10X high resolution infinity corrected objective (Edmund Optics, #58-372) with a 0.45 numerical aperture (NA) and 19-mm working distance (WD) was used to match the NA of GRIN lenses and provide enough working distance to avoid interference with the tetrode amplifier.

For two-photon fiber-coupled recording, we used a previously described<sup>15</sup> custom-built two-photon microscope with an Olympus UPlanXApo 10X objective (Olympus, PN N5701900) focusing the imaging laser on to the surface of a 1.5-m length Fujikura FIGH-15-600N coherent imaging fiber bundle. To obtain short pulses at the sample, the output of the MaiTai laser was sent through a 15-cm polarization-maintaining single-mode fiber (Thorlabs PN PM780-HP) for spectral broadening and then a grating pair compressor (600 lines/mm, Newport PN 33009BK02-351R) to correct for second order dispersion. The grating compressor has been slightly modified from the previously described system, using a 15-cm polarization-maintaining single-mode fiber and 800 lines/mm gratings. The end of the distal side of the coherent imaging fiber bundle is housed in a XYZ translator (Newport OC1-TZ, Newport OC1-LH1-XY) to allow alignment of the fiber bundle surface to the focus of the microscope objective.

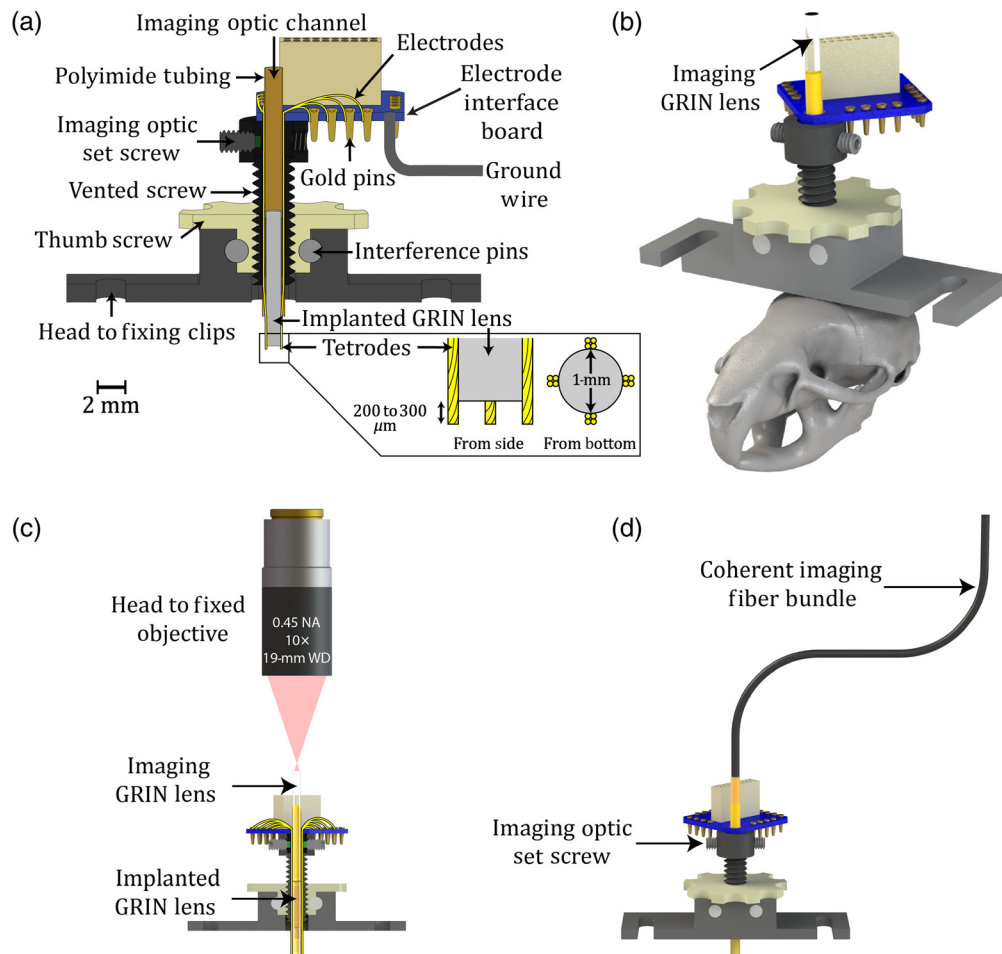


**Fig. 1** GRINtrode design. (a) Cross-section of the GRINtrode. The GRINtrode consists of four major components: an aluminum main body, a PEEK drive thumb screw, a stainless steel vented 4-40 socket head cap screw, and an EIB. The vented screw is threaded into the drive thumb screw, and the drive thumb screw is held in place by friction fitted Delrin interference pins. Flat sides are machined onto the vented screw, which interact with flat faces on the hole in the bottom of the aluminum body to create a vertical translation drive. Turning the drive thumb screw will increase the implantation depth of the GRINtrode probe without any rotation. The aluminum body includes an integrated head-fixing bar to improve head-fixed imaging stability and simplify the surgical procedure. Polyimide tubing is glued inside the vented screw and around GRIN lenses to provide a protected channel for tetrodes and isolate them from inserted imaging optics. The vented screw cap has threaded holes for nylon tipped #0-80 set screws that can be used to lock the imaging optic into place. Assembly instructions are provided in the [Supplementary Material](#). (b) Render of the GRINtrode as it would be used for head-fixed imaging to scale on a mouse skull. The GRINtrode weighs <3 g when fully assembled and is suitable for chronic implantation with stability demonstrated for up to 6 months. (c) Cross-section of the head-fixed GRINtrode imaging system. A 19-mm WD objective (Edmund Optics, #58-372) is used to avoid interference with the connector attached to the EIB. Additionally, a custom extension cord (Omnetics A71325-001) is used to further remove the Neuralynx RHD2132 amplifier from the imaging path. (d) Render of the GRINtrode in fiber-coupled modality as it would be used for recording from fiber-coupled freely moving animals. The fiber GRIN lens spacing is adjusted using a Sutter MPC-325 micromanipulator system, and the fiber is locked into place using the imaging optic set screw.

For one-photon fiber-coupled recording ([Supplementary Material](#)), we used a Nikon A1R confocal microscope with an Olympus UPlanXApo 10X objective focusing the excitation laser onto a 1.5-m-long Fujikura FIGH-15-600N coherent imaging fiber bundle. The proximal end of the Fujikura coherent imaging fiber bundle was coupled to a doublet GRIN lens (GRINtech NEM-100-25-10-860-DS) by gluing the fiber and the GRIN lens into a polyimide tube and then

inserted into the GRINtrode imaging optic channel. A XYZ translator (Thorlabs CXYZ1) allowed alignment of the fiber bundle surface to the microscope focus.

### 2.3 Tetrode Recording Setup

Tetrodes were passed through the GRINtrode and pinned into a Neuralynx EIB-16. A custom Omnetics cable harness (Omnetics A71325-001) was connected to the EIB-16 board and then to an Intan RHD2132 16 channel amplifier (Intan C3334). The custom harness was used to extend the connection to the amplifier away from the imaging GRIN lens such that it does not interfere with the imaging path. The amplifier was then connected to an Intan serial peripheral interface (SPI) cable (Intan C3206) and passes to an Intan RHD USB interface board (Intan C3100). The RHD USB interface board was connected to the recording computer with a USB cable. The Intan RHD USB interface also recorded a synchronization frame trigger output from the microscope so that imaging data and electrophysiology data could be time synced.

### 2.4 Image Processing

Head-fixed image timelapses were processed with the CaImAn software package for calcium image analysis.<sup>16</sup> CaImAn was used to perform motion correction, identify cell region of interests (ROIs), generate  $\Delta F/F$  traces of GCaMP fluorescence, and reconstruct denoised timelapses. Fiber coupled two-photon image timelapses were analyzed manually with Fiji<sup>17</sup> because the fiber bundle artifact prohibited analysis with CaImAn.

### 2.5 Tetrode Data Processing

Tetrode recordings are analyzed with inhouse MATLAB software (GitHub/restrepd/drta, GitHub/restrepd/drgMaster, and GitHub/ConMark/GRINtrode/Code) and the Wave\_clus software spike sorting package<sup>18</sup> modified as posted in GitHub/restrepd/wave\_clus. Each tetrode typically yields 0 to 3 single units in our findings.

### 2.6 Behavioral Video Analysis

Behavioral videos of freely moving animals were recorded at 30 fps using an infrared illuminated webcam (ELP-USBFHD01M-DL36). Behavioral videos were time synced to the imaging data by isolating the frames when the infrared light from the imaging laser first and last appeared. Behavioral kinematics were extracted using the DeepLabCut<sup>19</sup> markerless pose estimation software package.

### 2.7 Animals

Thy1-GCaMP6f mice<sup>20</sup> (JAX RRID:IMSR\_JAX:024276) were housed in a vivarium with a reversed light cycle of 14/10 hr light/dark periods with lights on at 10 p.m. Food (Teklad Global Rodent Diet No. 2918; Harlan) was available *ad libitum*. All experiments were performed according to protocols approved by the University of Colorado Anschutz Medical Campus Institutional Animal Care and Use Committee.

### 2.8 2.8 Surgery

Mice 2 to 5 months of age were anesthetized by brief exposure to isoflurane (2.5%), and subsequently, anesthesia was maintained with an intraperitoneal injection of ketamine (100 mg/kg) and xylazine (10 mg/kg). The mouse was then placed in a stereotaxic frame. A 1.6-mm diameter craniotomy was made above the target site using a dental drill. 1 to 2  $\mu$ L of adeno associated virus (pAAV1.Syn.GCaMP6s.WPRE.SV40 or pGP-AAV1.Syn.jGCaMP7f.WPRE) was injected 500  $\mu$ m above the target coordinates at a rate of 100 nL per minute. After the viral injection, tissue was aspirated<sup>21</sup> to  $\sim$ 500  $\mu$ m above the target coordinates, and the GRINtrode device was implanted at the target coordinates (see Sec. 3.3 for coordinates) using a motorized

micromanipulator (Sutter Instruments MPC-325). One ground screw was inserted 1-mm posterior from bregma and 1-mm lateral to the midline. The ground wire of the GRINtrode (A-M Systems Bare Silver Wire 0.008, Fisher Cat. No. NC0326296) was then wrapped around the ground screw and sealed with silver paint to optimize electrical contact (SPI Supplies PN 04999-AB). The ground screw and GRINtrode body were then sealed to the bone with C&B Metabond (Parkell SKU S380). Mice were allowed to recover for 4 weeks before the initiation of experiments and to allow time for virus expression.

### 3 Results

#### 3.1 GRINtrode

The GRINtrode is a head-mounted neural implant that uses a GRIN lens with surrounding tetrodes designed to provide simultaneous imaging of neuronal activity reported by GCaMP and recording of extracellular electrical neuronal activity [Fig. 1(a)]. This is achieved by simultaneous two-photon imaging through a GRIN lens and extracellular field potential recording provided by four tetrodes placed on the periphery of the GRIN lens. The GRINtrode design is based on the optetrode<sup>22</sup> with a modified housing and bracket to allow for head-fixed or multicore fiber-coupled freely moving imaging and utilizing a GRIN lens instead of an optical fiber for imaging [Figs. 1(b) and 1(c)]. By utilizing a GRIN lens and tetrode-based design, we provide a solution for simultaneous optical imaging and extracellular electrophysiology from deep brain structures using either head-fixed one-photon or two-photon microscopy. Additionally, the GRINtrode imaging system can be coupled to a coherent imaging fiber bundle<sup>15</sup> [Fig. 1(d)] to allow for fiber-coupled freely moving one-photon (Fig. S1 in the [Supplementary Material](#)) or two-photon microscopy (Fig. 5) using a coherent imaging fiber bundle<sup>15</sup> with simultaneous extracellular electrophysiology.

#### 3.2 Optical GRINtrode Characterizations

Head-fixed two-photon GRINtrode imaging was performed by inserting a GRIN lens into the imaging optic channel of the GRINtrode and imaging through two GRIN lenses in series. In the data presented, we used two different combinations of GRIN lenses. For imaging system A, the chronically implanted GRIN lens is a GRINtech 1-mm diameter, 9-mm-long GRIN lens (GRINtech NEM-100-25-10-860-S-1.0p), and the imaging GRIN lens is a GRINtech 1-mm diameter, 14-mm-long GRIN lens (GRINtech NEM-100-25-10-860-S-1.5p). For imaging system B, the chronically implanted GRIN lens is an Inscopix 1-mm diameter, 9-mm-long GRIN lens (Inscopix 1050-002177), and the imaging GRIN lens is a GRINtech 0.85-mm diameter, 10.8-mm-long GRIN lens (GRINtech NEM-085-45-10-860-S-1.5p). The smaller 0.85-mm diameter imaging GRIN lens in imaging system B was used for an early iteration of the GRINtrode where the polyimide tubing used to create the imaging optic channel was too small in diameter to allow for 1-mm diameter imaging GRIN lenses to be inserted. System A is used in a later iteration of the device, which allows the use of 1-mm imaging GRIN lenses for larger FOV. System A also uses GRINtech lenses rather than Inscopix lenses for the implanted lens due to more transparent specifications and availability of Zemax models.

Two-photon imaging characteristics of the GRINtrode imaging systems were measured by imaging calibration targets at an excitation wavelength of 920 nm and emission collected through a 525/50 nm bandpass filter (Semrock PN FF03-525/50-25). Magnification was characterized by imaging a 50- $\mu$ m grid slide calibration target (Max Levy II-VI Aerospace and Defense, DA113) without GRIN lens imaging systems and calibrating the pixels/micron of the image, then imaging the 50- $\mu$ m grid slide through GRIN lens imaging systems and measuring the factor by which pixels/micron was impacted. The field of view (FOV) was measured by imaging the 50- $\mu$ m grid slide [Figs. 2(a1) and 2(b1)], subtracting the baseline fluorescence and counting the number of peaks from the grid slide fluorescence profile that exceeded 10% of the maximum fluorescence intensity. The lateral resolution of the GRINtrode imaging systems was characterized by imaging 0.5- $\mu$ m diameter fluorescent beads (ThermoFisher G500) (Figs. 2(a2)

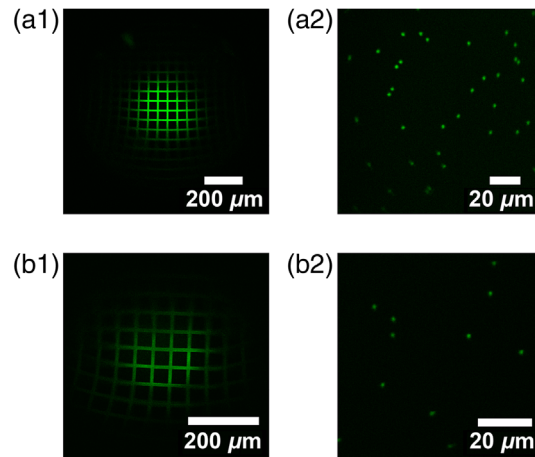


**Fig. 2** Two-photon optical characterizations of the GRINtrode imaging systems at 920 nm. 50- $\mu\text{m}$  grid slide calibration target used for FOV measurements using the GRIN lens imaging system A (a1) and imaging system B (b1). 0.5- $\mu\text{m}$  fluorescent bead slide sample used for lateral and axial FWHM measurements using the GRIN lens imaging system A (a2) and imaging system B (b2).

and 2(b2)] and calculating the average full width half maximum (FWHM) of Gaussian fits to the line profiles of five randomly sampled beads. Lateral FWHM was then corrected for magnification by multiplying the measured lateral FWHM by a factor of  $1/M$ . The axial resolution of the GRINtrode imaging systems was characterized by taking a  $Z$ -stack of the 0.5- $\mu\text{m}$  diameter fluorescent beads and calculating the average FWHM of Gaussian fits to the  $Z$  axis profiles of five randomly sampled beads.  $Z$ -stacks were performed by moving the objective axially with a static GRIN lens imaging system and static sample such as to recreate how a  $Z$ -stack would be performed with the actual device where the GRIN lens imaging system cannot be moved axially along with the objective. Axial FWHM was then corrected for magnification by multiplying the measured axial FWHM by a factor of  $1/M^2$ . The results are summarized in Table 1.

Interestingly, we found that magnification varies with GRIN lens system to sample spacing and objective spacing with magnification being more pronounced in system B, which uses a smaller diameter imaging lens versus implanted lens. Zemax simulations support this finding (Fig. S2 in the [Supplementary Material](#)). To ensure the correct magnification factor was used for corrections to lateral and axial FWHM, the 50- $\mu\text{m}$  grid target used to measure magnification and 0.5- $\mu\text{m}$  beads used to measure lateral and axial FWHM were imaged at the same GRIN lens to sample spacing.

### 3.3 Two-Photon Head-Fixed GRINtrode Recording

We used the GRINtrode to perform simultaneous *in vivo* two-photon imaging at 920-nm excitation and extracellular electrical recording. The GRINtrode was inserted into the brain at two different stereotaxic coordinates from bregma [anterior–posterior (AP):  $-2.4$  mm, medial–lateral (ML):  $+1.8$  mm, and dorsal–ventral (DV):  $-1.5$  mm for animal A; AP:  $-3.16$  mm, ML:  $+2.5$  mm, and DV:  $-1.75$  mm for animal B] and was advanced in a dorsoventral trajectory from the neocortex targeting dentate gyrus for animal A and hippocampal layer CA1 for animal B.

**Table 1** Table summarizing results for optical characterizations using the 50- $\mu\text{m}$  grid slide for magnification and FOV and 0.5- $\mu\text{m}$  fluorescent beads for lateral and axial FWHM measurements.

	Magnification	FOV ( $\mu\text{m}$ )	Lateral FWHM ( $\mu\text{m}$ )	Axial FWHM ( $\mu\text{m}$ )
System A	1.07	400	1.63	32.56
System B	1.89	350	0.62	17.74

GCaMP (pGP-AAV1.Syn.jGCaMP7f.WPRE for animal *A* and pAAV1.Syn.GCaMP6s.WPRE.SV40 for animal *B*) was virally expressed in neurons using adeno-associated viruses expressing the sensor under the hSyn promoter. Additionally, GCaMP was expressed transgenically in the Thy1-GCaMP6f mice used. We used both transgenic and viral GCaMP expression to maximize chances of obtaining GCaMP signal per surgery as the goal of this work was to demonstrate feasibility of the GRINtrode device; use of a more specific GCaMP expression protocol will be crucial when addressing questions regarding unique cell-type function.

Two-photon head-fixed imaging was performed using a home-built Sutter Instruments movable objective microscope (Sec. 2.2), and tetrode recording was performed using an Intan RHD2000 system (Sec. 2.3). Figure 3 shows images of GCaMP fluorescence, traces of fluorescence intensity for a subset of the ROIs and simultaneous electrophysiology data. The FOVs showed 40 and 100 areas for datasets *A* and *B*, respectively, with fluctuating intensity above background that was classified as different components using CaImAn [Figs. 3(a1) and 3(b1)]. Raw versus CaImAn-processed  $\Delta F/F$  traces of GCaMP activity are shown in Figs. 3(a2) and 3(b2). CaImAn-processed  $\Delta F/F$  traces for all ROIs shown in Figs. 3(a1) and 3(b1) are shown in Figs. 3(a3) and 3(b3), respectively. The wavelet power spectrogram showed increases in power that took place at low frequency as expected [Figs. 3(a4) and 3(b4)]. Raw electrode recordings from one electrode of each tetrode are shown in Figs. 3(a5), 3(a6), 3(b5), and 3(b6).

### 3.4 Cross-Correlation Analysis of GCaMP and LFP Data

GCaMP fluorescence of neurons imaged by the GRINtrode is expected to be directly related to action potential firing.<sup>5,16,23,24</sup> What would be the relationship of this optical recording of neuronal activity to the low frequency bandwidth (1 to 100 Hz) LFP recorded by the surrounding tetrodes? The LFP recorded by the tetrodes is generated by postsynaptic potentials in nearby neurons.<sup>4</sup> Interestingly, the LFP does not simply reflect the activity of nearby neurons, because postsynaptic potentials that generate local current dipoles will result from the firing of nearby neurons forming local recurrent connections as well as the firing of remote neurons with afferent inputs into a region, and because there is a contribution to the LFP from distant signals through volume conduction.<sup>4,25,26</sup> As a result, it is expected that optical GCaMP and LFP data from the GRINtrode should be partially overlapping.

To evaluate overlap between optical recordings from specific cells and LFP recordings, we performed cross-correlation analysis on the data presented in Fig. 3(b) computing the Pearson's linear correlation coefficient between single component  $\Delta F/F$  traces of GCaMP fluorescence and the LFP power traces per electrode. LFP data were split into four bandwidths<sup>27</sup>: theta (6 to 14 Hz), beta (15 to 30 Hz), low gamma (35 to 55 Hz), and high gamma (65 to 95 Hz). Cross-correlation was then computed between all 100 GCaMP traces for the timelapse and each of these 4 bandwidths for all 16 electrodes. Figure 4(c) shows  $\Delta F/F$  traces of the four optically recorded cells with the highest correlation coefficients to the theta bandwidth LFP data. Figures 4(b) and 4(d) show the histograms of the correlations between all pairs of LFP power and GCaMP  $\Delta F/F$  traces (original histograms) compared with histograms for correlations calculated after time shuffling of the  $\Delta F/F$  traces for the theta bandwidth. Shuffling was performed 100 times by a circular shift of the trace by a random number of time points with a minimum shift of one tenth of the length of the trace. The original histograms are skewed toward positive correlations indicating that a subset of these pairwise cross-correlations are positively correlated. Indeed, when tested for significance using a Kolmogorov–Smirnov (KS) test, we find that the original histograms differ from the shuffled histograms (KS test  $p$  value < 0.001). Furthermore, 75% to 90% of the correlations computed between the LFP power and  $dF/F$  traces yield  $p$  values below a significance  $p$  value adjusted using the false discovery rate to correct for multiple comparisons<sup>28</sup> [Fig. 4(f)]. Spike sorting results for the tetrode, which yielded the single unit shown in Fig. 4(e), are shown in Fig. 4(g).

#### 3.4.1 Cross-correlation analysis of GCaMP and spike data

Because spiking activity from multiple neurons neighboring an electrode contributes to the high frequency (500 to 5000 Hz) filtered field potential,<sup>2–4</sup> it may theoretically be possible to record



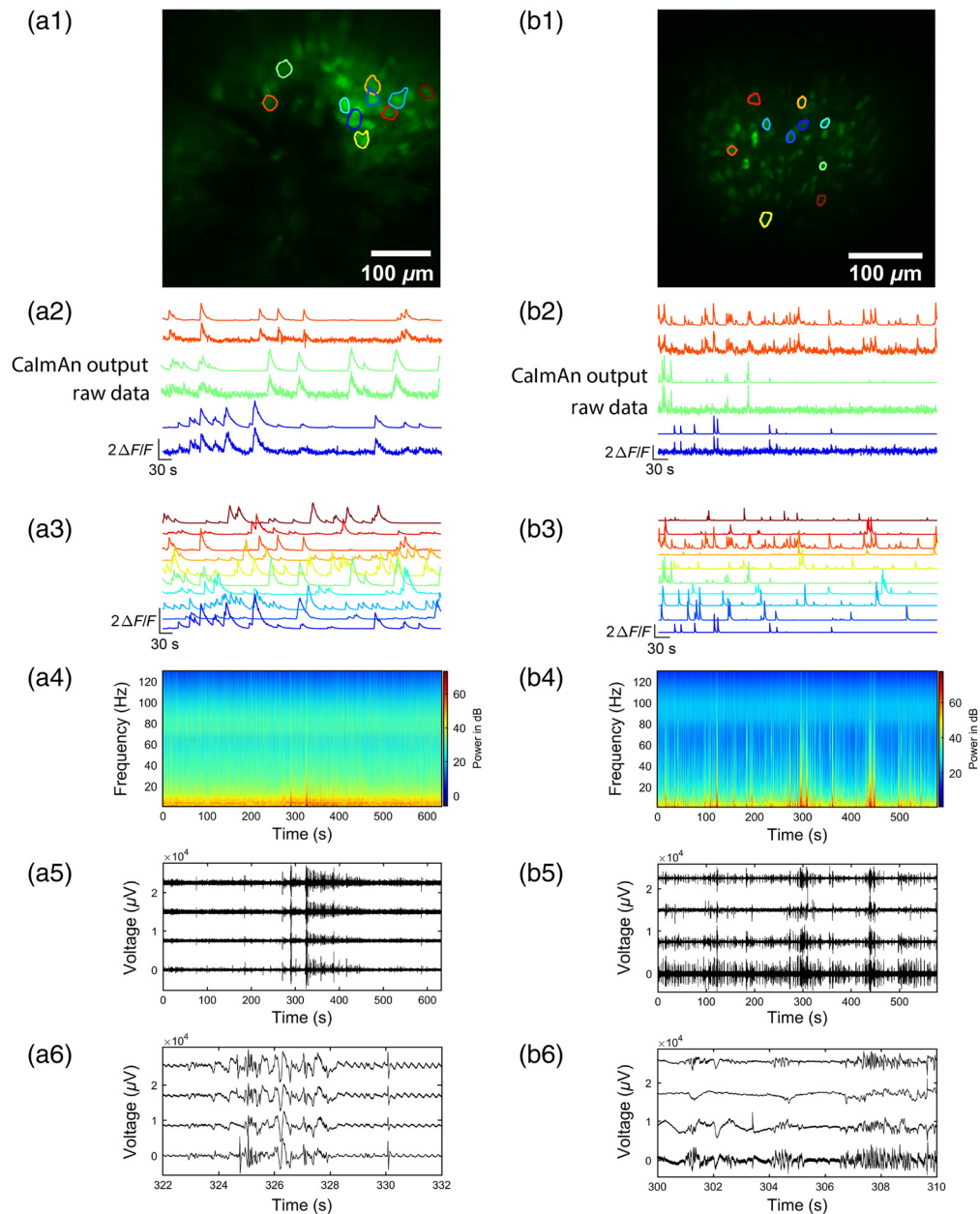


**Fig. 3** Example GRINtrode data recorded from head-fixed mice. (a1) Maximum intensity timelapse projection of GCaMP data from a 10-min recording session in a female Thy1xGCaMP6f mouse with viral expression of jGCaMP7f imaged with GRIN lens system A. The GRINtrode was implanted to dentate gyrus. Selected cell ROIs are outlined. (a2)  $\Delta F/F$  traces of raw GCaMP imaging data versus CalmAn-processed data, color matched to ROIs of selected cells in panel (a1). (a3) CalmAn-processed  $\Delta F/F$  traces of GCaMP fluorescence, color matched to ROIs in panel (a1). (a4) Power spectrogram of LFP activity, averaged over all 16 electrodes of the GRINtrode for the recording session. (a5) Raw electrode recordings selected from one electrode of each tetrad. (a6) Raw electrode recordings from the same electrodes shown in panel (a5) over a shorter time span of high LFP activity. (b1) Maximum intensity timelapse projection of GCaMP data from a 10-min recording session in a female Thy1xGCaMP6f mouse with viral expression of GCaMP6s imaged with GRIN lens system B. The GRINtrode was implanted to hippocampal layer CA1. Selected cell ROIs are outlined. (b2)  $\Delta F/F$  traces of raw GCaMP imaging data versus CalmAn-processed data, color matched to ROIs of selected cells in panel (b1). (b3) CalmAn-processed  $\Delta F/F$  traces of GCaMP fluorescence, color matched to ROIs in panel (b1). (b4) Power spectrogram of LFP activity, averaged over all 16 electrodes of the GRINtrode for the recording session. (b5) Raw electrode recordings selected from one electrode of each tetrad. (b6) Raw electrode recordings from the same electrodes shown in panel (b5) over a shorter time span of high LFP activity.

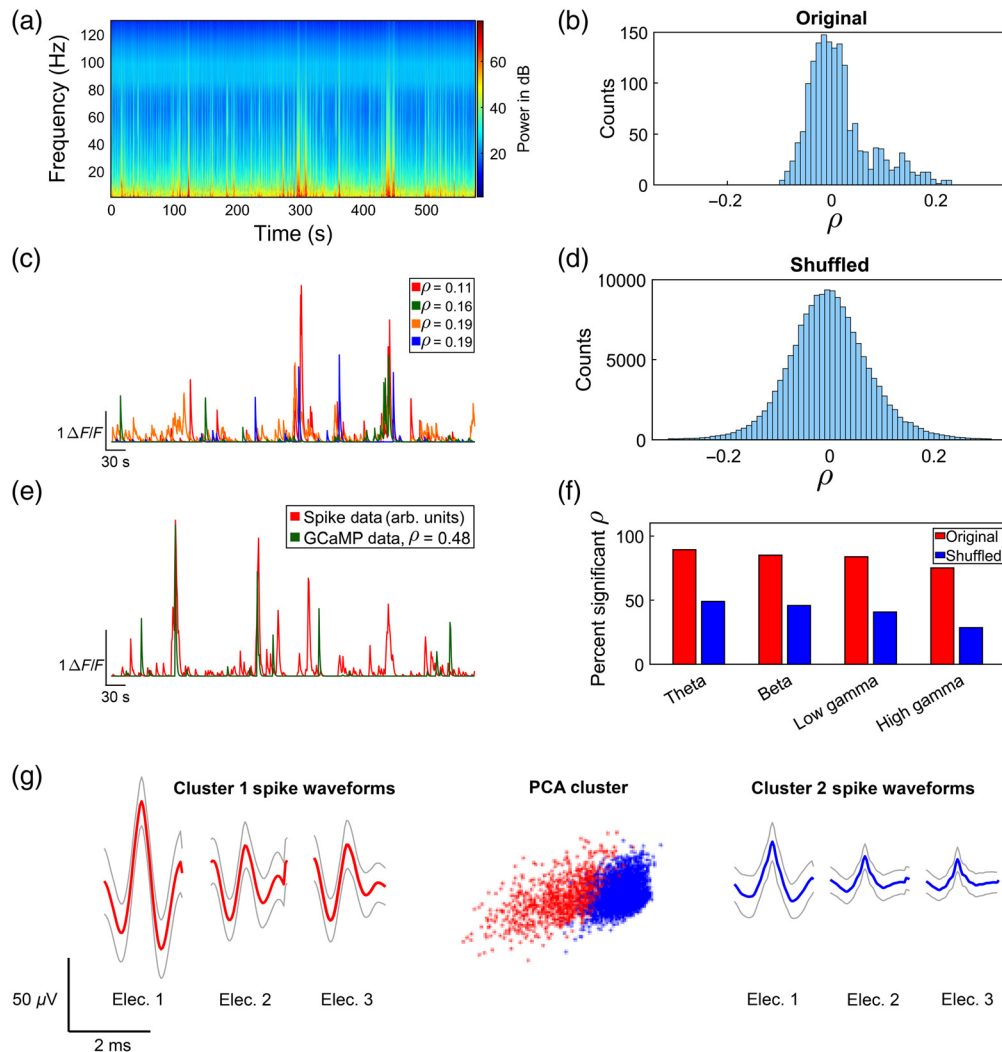


**Fig. 4** GCaMP versus electrical data cross-correlation results analyzing data in Fig. 3(b). (a) Mean LFP power spectrogram of all 16 electrodes during a 10-min timelapse. (b) Histogram of Pearson linear correlation coefficients between all 100 GCaMP cells and all 16 electrodes for the theta bandwidth, showing a skew towards positive correlations. (c) CalmAn-processed  $\Delta F/F$  traces of the four optically recorded cells with highest correlation coefficients to the theta bandwidth LFP data. The legend reports the average  $\rho$  for that GCaMP trace across all 16 electrodes. (d) Histogram of Pearson linear correlation coefficients between shuffled GCaMP cells and all 16 electrodes for the theta bandwidth, showing a more normal distribution than the original, non-shuffled cross-correlation analysis histogram. (e) Cross-correlation analysis results between CalmAn-processed GCaMP data and convolved spike data using Fig. 3(b) data. Binary spike data were convolved with an exponential decay function using the same decay constant used in CalmAn analysis to approximate what the activity of these spiking cells would look like as GCaMP signal. We then used Pearson's linear correlation coefficient to find the optically recorded cells, which matches the processed spike data most closely. Here, we are showing with the highest correlation coefficient,  $\rho = 0.475$ . The units of the spike data are arbitrary, so we have scaled the spike data trace to be of similar amplitude to the GCaMP trace. (f) Bar chart showing per bandwidth percentage of significant correlations for Pearson correlation coefficient analysis for original and shuffled datasets. (g) Spike waveform and PCA cluster results from spike sorting on the tetrode, which yielded the highest correlation single unit shown in panel (e), shown in red. Gray traces show  $\pm$  standard deviation of the waveform. The fourth electrode was used as a reference and hence did not yield a waveform.

the same neuron both optically and electrically using the GRINtrode if the electrical and optical recording fields are overlapping. There are challenges in achieving overlapping optical and electrical fields though. The recording plane of the tetrodes relative to the imaging plane is determined by the length of tetrode that extends past the implanted GRIN lens. We attempt to make this length as close to the working distance of the GRINtrode imaging system as possible; however, because tetrodes are cut by hand, there is variability in this parameter. Additionally, tetrodes are fixed on the periphery of the GRIN lens, 500  $\mu\text{m}$  laterally from the center of the imaging field and provide a theoretical recording sphere radius of 100  $\mu\text{m}$ .<sup>29</sup> With an FOV of  $\sim 450 \mu\text{m}$ , overlap between optical and electrical recording fields is not expected. Still, it may be the case that optical and electrical single units display correlated activity even though they come from different recording fields. With these caveats in mind, we proceeded to explore the relationship between single unit electrical activity and GCaMP fluorescence changes. We extracted single unit activity from electrical recordings using a custom implementation<sup>30</sup> of the `wave_clus` software package.<sup>18</sup> The software outputs a binary time series with single unit spike timings represented as a one. After extracting spikes, we then convolved this binary series with an exponential decay function using the same decay constant used in the `CaImAn`<sup>16</sup> analysis of the optical recordings to approximate what the spike activity would look like converted to a GCaMP signal. We then performed cross-correlation analysis using Pearson's linear correlation coefficient to seek out optically recorded cells that match closest to the processed spiking activity. Figure 4(e) shows that the convolved firing of one isolated single unit displays a Pearson correlation coefficient of 0.48. The spike and GCaMP data show two temporally localized transients, but several spike transients that are not accounted for by the GCaMP data. We suspect this is because the isolated "single unit" was not in the imaging plane and displayed correlated spiking with units in the imaging plane, perhaps connected through a neuronal network.

### 3.5 Freely Moving Fiber-Coupled Two-Photon GRINtrode Recording

We performed freely moving two-photon imaging using a 1.5-m-long Fujikura FIGH-15-600N coherent imaging fiber bundle inserted into the imaging optic channel.<sup>15</sup> A single mode fiber and grating-pair compressor were used to correct for the linear and nonlinear dispersion of fiber bundle (see Sec. 2), allowing short pulses at the sample. This setup allowed us to perform simultaneous two-photon imaging of GCaMP activity and extracellular electrophysiology with the GRINtrode in a freely moving mouse. The GRINtrode was inserted into the brain at stereotaxic coordinates (AP:  $-2.4 \text{ mm}$ , ML:  $+1.8 \text{ mm}$ , and DV:  $-1.25 \text{ mm}$ ) referenced to bregma in a 3-month-old Thy1-GCaMP6f mouse and was advanced in a dorsoventral trajectory from the neocortex, targeting the CA1 layer of the hippocampus. The calcium sensor jGCaMP7f was expressed in neurons using AAV under the `hSyn` promoter. Two-photon fiber-coupled freely moving imaging was performed using a custom-built microscope (Sec. 2.2), and tetrode recording was performed using an Intan RHD2000 system (Sec. 2.3). A Sutter MPC-325 micromanipulator system was used to fine adjust the Z spacing between the chronically implanted GRIN lens inside of the GRINtrode and the coherent imaging fiber bundle, and the fiber bundle was locked in place using the imaging optic set screws.

The mouse movement was recorded with a camera, whereas simultaneous acquiring two-photon imaging [Figs. 5(a) and 5(c)] and LFP recording [Figs. 5(e) and 5(f)] as the mouse foraged through a cage with food pellets [Fig. 5(b) and Video 1]. We extracted behavioral kinematics using the `DeepLabCut` software package.<sup>19</sup> Figures 5(c), 5(e), and 5(f) show temporally synchronized GCaMP fluorescence intensity traces, raw electrode traces, and LFP spectrogram, whereas the mouse foraged through the cage. Figure 5(h) shows the head velocity of the mouse during the recording session. Figure 5(d) shows the mouse's position over the timelapse with the location during transients marked by a color-coded dot matching the ROI and trace colors in Figs. 5(a) and 5(c). Figure 5(g) shows Gaussian-smoothed ( $\sigma = 62.5 \text{ pixels}$ ) spatial heatmaps of cell activity according to cell numbers in Fig. 5(c) across 25 pixel-by-25 pixel bins normalized by time spent per bin. Analysis using the two-dimensional KS test shows all heatmaps are significantly different from one another. Together, these results demonstrate the utility of the GRINtrode in providing simultaneous two-photon imaging and extracellular electrophysiology in a freely moving mouse.

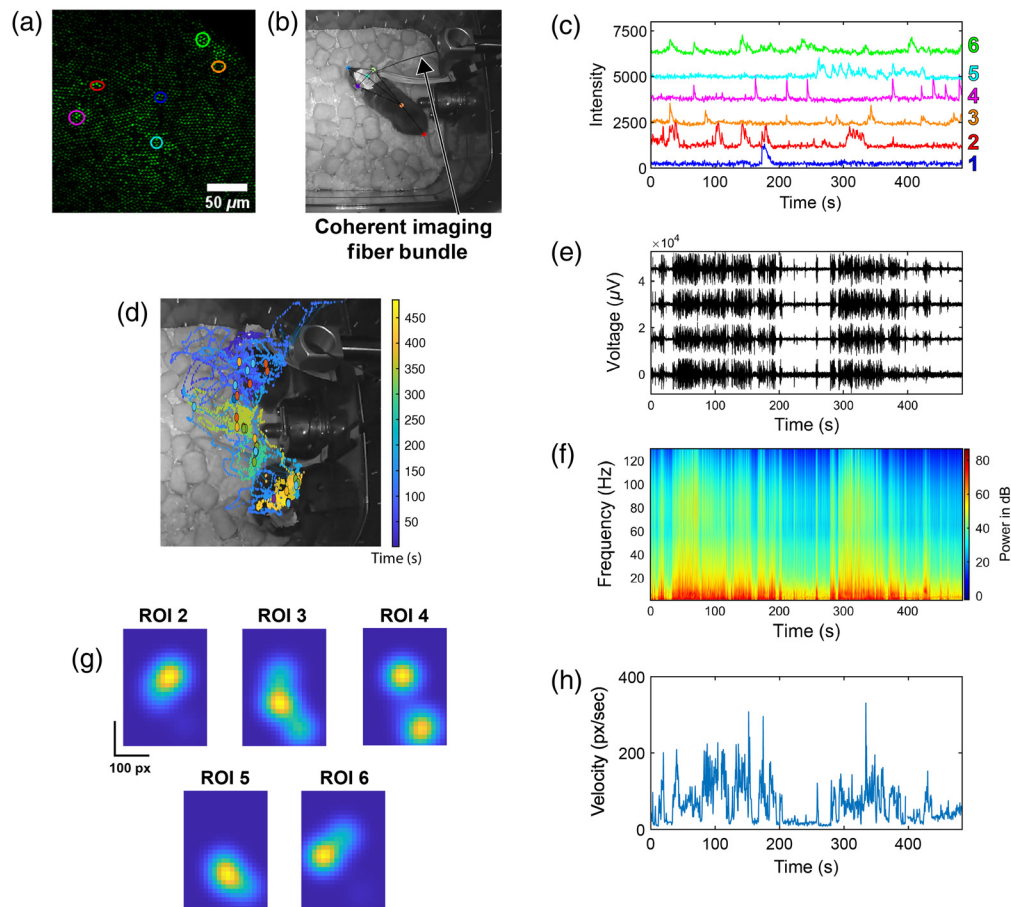


**Fig. 5** Fiber-coupled freely moving two-photon GRINtrode recording. (a) Standard deviation timelapse projection of an 8-min recording session, and highlighted ROIs are color matched to traces in panel (b). (b) Still frame of behavioral video ([Video 1](#)) showing fiber-coupled freely moving animal and markers generated by analysis with DeepLabCut ([Video 1](#), MP4, 17.211 MB; [URL: <https://doi.org/10.1117/1.NPh.9.4.045009.s1>]). (c) Color-matched fluorescence intensity traces from ROIs in panel (a). (d) Mouse head position, color coded to time over the course of the timelapse, overlaid on an image showing the mouse during the first and last frame of recording. Mouse position during calcium transients is shown as dots color coded to ROIs in panel (a) and traces in panel (c). Activity in the top right of the frame shows the position of the head as the mouse stood upright to investigate the top corner of the cage. (e) Raw electrode recording from one electrode of each tetrode of the GRINtrode. (f) Mean LFP power spectrogram of all 16 electrodes. (g) Normalized spatial heatmaps of cell activity, according to cell numbers in panel (c). (h) Velocity of the head of the mouse during the behavioral video generated by DeepLabCut analysis.

Fiber coupling the animal in addition to the electrophysiology data cable presents the concern of limitation of movement as cables may twist. However, the dominant factor limiting movement is the torsional resistance of the imaging fiber bundle. The mouse was able to navigate freely subject to the length of the fiber bundle, but torsional resistance in the fiber limits the animal's ability to rotate. The animal was still able to achieve a full 360-deg rotation. The fiber is also subject to a minimum 30-mm bending radius, which did not present a limitation to movement.

## 4 Discussion

We developed and validated a GRINtrode, the first GRIN lens and tetrode-based head-mounted neural implant designed for simultaneous two-photon calcium imaging and extracellular electrophysiology. Importantly, we have demonstrated the feasibility of fiber coupling the GRINtrode to allow imaging and electrical recording of neural activity in the freely moving mouse. Simultaneously, recording neural activity with optical and electrical modalities provides a unique

opportunity to probe the relationship between these recording methods *in vivo*. We have demonstrated positive correlation between optically and electrically recorded activity by performing cross-correlation analyses between the two data types.

#### 4.1 Extracellular Field Potential Electrophysiology

Extracellular field potential recordings are the oldest method of recording *in vivo* neural activity, and as such there is an abundance of knowledge based on this technique. Therefore, it is desirable for neurophysiologists to collect optical data with simultaneous electrophysiology *in vivo* to build upon prior knowledge obtained in systems neuroscience. By placing electrodes into the brain tissue, researchers can record a direct measure of neural activity relayed in the form of action potentials. Action potentials create current sinks and sources whose flow through the resistive extracellular compartment is detected as voltage changes at the recording site. The recording site of single electrodes can be used to capture neural oscillations, a signature of coordinated dynamics in the brain<sup>4,31</sup> generated by the activity of large ensembles of neurons. Whereas such information is crucial to decoding the underlying rhythms of the brain, such recordings have a trade-off of high temporal resolution and poor spatial resolution.<sup>32</sup> In coupling with optical methods, researchers can simultaneously explore the relationship between single cell responses and network ensembles, revealing new insights into brain state dynamics at an intermediary scale.

#### 4.2 Optical Neural Activity Recording

Optical methods of recording *in vivo* neural activity are a relatively new method in the field of neuroscience that has become popular because they allow recording from large ensembles of spatially resolved neurons.<sup>11,33–36</sup> Optically recording neural activity requires a fluorescent reporter whose fluorescence intensity is modulated by neural activity. There are several classes of these reporters: calcium indicators, neurotransmitter indicators, and voltage indicators. In this work, we focus on the use of the widely used calcium indicator, GCaMP.<sup>24</sup>

Optical recording methods are subject to some limitations due to the scattering nature of brain tissue, restricting imaging depth. However, there are methods to overcome these limitations. Multiphoton imaging uses longer wavelength excitation light, such that multiple coincident photons are needed to excite the fluorophore. The use of longer near-infrared wavelengths increases optical penetration due to reduced scattering compared with visible wavelengths. Multiphoton imaging also provides optical sectioning, as the probability of fluorophore excitation depends on intensity, which is confined to the focus of the imaging system.

In addition, scattering tissue can be bypassed by implanting imaging optics in deep brain regions. The GRIN lenses are rod-shaped lenses, which provide optical power by means of a radially dependent index of refraction. These lenses are useful for *in vivo* neural imaging in deeper brain regions that are otherwise not optically accessible due to the limited penetration depth of optical imaging. Their small form factor allows them to be chronically implanted above the ROI.<sup>21</sup> One significant trade-off of this approach is the invasiveness of implantation, and the surgical skill needed to capture optical responses *in vivo*. GRIN lens implantation requires traumatic surgeries in rodents where the surgeon aspirates superficial structures above the ROI prior to GRIN lens insertion. However, when using proper surgical techniques during implantation, the datasets collected with the GRINtrode are rich and can convey unseen data compared with use of a single neural recording modality alone. Therefore, the larger need to record electrical and optical activities at cellular and network resolution in deep brain regions can be performed using the GRINtrode, yet its insertion with minimal disturbance to brain structures superficial to the recording site remains impossible for now.

The GRINtrode imaging system is comprised of two GRIN lenses: the implanted lens and the imaging lens. The imaging lens is easily removable and can be switched, which allows for changes to the GRINtrode imaging system. For instance, in our findings, we discovered that using a smaller diameter imaging lens as in imaging system B increases magnification of the imaging system. Imaging system A, using a larger diameter imaging lens, offers improved FOV. The GRINtrode allows the user to make a choice between magnification and FOV, which can be switched quickly and easily.

Optical characterization of the imaging systems also shows that imaging system B, composed of a 10.8-mm-long by 0.85-mm diameter imaging GRIN lens and a 9-mm-long by 1-mm diameter implanted GRIN lens, performed better in lateral and axial resolution and introduced magnification. These improvements were not expected and their cause is not entirely clear.

Optical techniques often require head-fixing the animal to perform imaging, limiting the behavioral paradigms capable of being investigated. If the entire imaging system can be miniaturized to the extent that the animal can carry it, freely moving wireless imaging is possible.<sup>37</sup> This is currently limited to one-photon imaging modalities though, as sufficiently miniaturized coherent laser sources are not available. However, it is possible to use optical fibers to fiber couple imaging systems and allow for multiphoton imaging in freely moving animals.<sup>15</sup>

### 4.3 Bringing Together the Information Encoded by LFP Recording and Optical Imaging of Neuronal Activity

Extracellular LFP recording has provided important information on the behavioral relevance and circuit mechanisms of neural function.<sup>4,27,38,39</sup> High-frequency bandwidth recordings (500 to 5000 Hz) yield information on single neuron activity particularly when recording is performed with multiunit electrodes making it more convenient to isolate single units.<sup>14,40</sup> Furthermore, lower frequency bandwidth LFP (1 to 250 Hz) also provides key information on neural circuits although understanding of the relationship between the LFP, and the activity of single neurons is difficult because of a lack of a well-posed inverse model to determine single unit activity based on conservation of charge and Maxwell's equations.<sup>4</sup> Development of miniature devices that allow simultaneous imaging of neural activity and electrical recording of the LFP provides the new tools to understand the relationship between the LFP and single neuron activity and provides the opportunity to use closed-loop modulation based on either the LFP or on single-unit activity and find the consequence on neural activity and behavior.<sup>38,39,41</sup>

Our GRINtrode device provides the opportunity for simultaneous optical imaging and field potential recording in the freely moving animal. Tetrodes are bundles of four electrodes, which provide multiple recording sites with a  $\sim 20\text{-}\mu\text{m}$  spatial separation. These multiple recording sites allow for isolation of single unit spiking activity as spike amplitude is a function of distance to the recording site. However, use of tetrodes limits the number of single units that can be isolated and the ability to achieve overlapping optical and electrical fields. Future versions can incorporate patterned multielectrode devices to provide extraction of more single units and accurate control over relative placement of optical and electrical recording fields.

## 5 Conclusion

We demonstrated a robust, easy to construct neural implant, the GRINtrode, that allows for simultaneous optical and electrical recording of neuronal activity *in vivo*. It is suitable for head-fixed 1-photon or 2-photon optical recording with simultaneous extracellular electrophysiology provided by 16 electrodes grouped into 4 tetrodes. We also demonstrated two-photon fiber-coupled GRINtrode recording, allowing use in freely moving animal recording.

There has been increasing effort to develop methods for simultaneous optical and electrophysiological recording of neural activity *in vivo*. There is abundant motivation to develop and improve methods for performing this recording: investigating GCaMP dynamics versus direct electrical recordings of single unit activity, using electrical recording to compensate for the limits on temporal resolution intrinsic to optical methods, development of closed-loop optogenetic systems based on LFP activity, etc. The GRINtrode presents a versatile solution to this desire for bimodal recording, it is easy to construct and uses a common method for electrical recording and allows for advanced optical techniques such as multiphoton imaging and freely moving recording by means of fiber coupling capability.

## Disclosures

The authors have declared they have no conflicts of interest.

## Acknowledgments

This research was supported by an Administrative Supplement to NIH U01 NS099577, NIH UF1 NS116241, NIH R01 DC000566, NIH T32DC012280, and NSF BCS-1926676. Polyimide tubing was courteously provided by MicroLumen, Inc.

## 6 Code, Data, and Materials Availability

The authors have made code used for analysis presented in this article available for access through GitHub/restrepd/drta, GitHub/restrepd/drgMaster (<https://github.com/restrepd>), and GitHub/ConMark/GRINtrode/Code (<https://github.com/ConMark/GRINtrode>). Data presented in this manuscript are available for access through author request. CAD models of GRINtrode components are available for access through GitHub/ConMark/GRINtrode/CAD (<https://github.com/ConMark/GRINtrode>).

## References

1. E. D. Adrian, "The electrical activity of the mammalian olfactory bulb," *Electroencephalogr. Clin. Neurophysiol.* **2**, 377–388 (1950).
2. C. Bédard, H. Kröger, and A. Destexhe, "Modeling extracellular field potentials and the frequency-filtering properties of extracellular space," *Biophys. J.* **86**, 1829–1842 (2004).
3. G. Buzsáki, C. A. Anastassiou, and C. Koch, "The origin of extracellular fields and currents — EEG, ECoG, LFP and spikes," *Nat. Rev. Neurosci.* **13**, 407–420 (2012).
4. B. Pesaran et al., "Investigating large-scale brain dynamics using field potential recordings: analysis and interpretation," *Nat. Neurosci.* **21**, 903–919 (2018).
5. T. W. Chen et al., "Ultrasensitive fluorescent proteins for imaging neuronal activity," *Nature* **499**, 295–300 (2013).
6. Z. Wu, D. Lin, and Y. Li, "Pushing the frontiers: tools for monitoring neurotransmitters and neuromodulators," *Nat. Rev. Neurosci.* **23**, 257–274 (2022).
7. T. Knöpfel and C. Song, "Optical voltage imaging in neurons: moving from technology development to practical tool," *Nat. Rev. Neurosci.* **20**, 719–727 (2019).
8. J. Platisa and V. A. Pieribone, "Genetically encoded fluorescent voltage indicators: are we there yet?" *Curr. Opin. Neurobiol.* **50**, 146 (2018).
9. E. Salinas and T. J. Sejnowski, "Correlated neuronal activity and the flow of neural information," *Nat. Rev. Neurosci.* **2**, 539–550 (2001).
10. M. Thunemann et al., "Deep 2-photon imaging and artifact-free optogenetics through transparent graphene microelectrode arrays," *Nat. Commun.* **9**, 2035 (2018).
11. D. Aharoni et al., "All the light that we can see: a new era in miniaturized microscopy," *Nat. Methods* **16**, 11–13 (2018).
12. X. Wu et al., "A modified miniscope system for simultaneous electrophysiology and calcium imaging in vivo," *Front. Integr. Neurosci.* **15**, 21 (2021).
13. L. F. Cobar et al., "Opto-electrical bimodal recording of neural activity in awake head-restrained mice," *Sci. Rep.* **12**, 736 (2022).
14. C. M. Gray et al., "Tetrodes markedly improve the reliability and yield of multiple single-unit isolation from multi-unit recordings in cat striate cortex," *J. Neurosci. Methods* **63**, 43–54 (1995).
15. B. N. Ozbay et al., "Three dimensional two-photon brain imaging in freely moving mice using a miniature fiber coupled microscope with active axial-scanning," *Sci. Rep.* **8**, 8108 (2018).
16. A. Giovannucci et al., "CaImAn an open source tool for scalable calcium imaging data analysis," *eLife* **8**, e38173 (2019).
17. J. Schindelin et al., "Fiji: an open-source platform for biological-image analysis," *Nat. Methods* **9**, 676–682 (2012).
18. R. Q. Quiroga, Z. Nadasdy, and Y. Ben-Shaul, "Unsupervised spike detection and sorting with wavelets and superparamagnetic clustering," *Neural Comput.* **16**, 1661–1687 (2004).

19. A. Mathis et al., “DeepLabCut: markerless pose estimation of user-defined body parts with deep learning,” *Nat. Neurosci.* **21**, 1281–1289 (2018).
20. H. Dana et al., “Thy1-GCaMP6 transgenic mice for neuronal population imaging in vivo,” *PLoS One* **9**, e108697 (2014).
21. S. L. Resendez et al., “Visualization of cortical, subcortical and deep brain neural circuit dynamics during naturalistic mammalian behavior with head-mounted microscopes and chronically implanted lenses,” *Nat. Protoc.* **11**, 566–597 (2016).
22. P. Anikeeva et al., “Optetrode: a multichannel readout for optogenetic control in freely moving mice,” *Nat. Neurosci.* **15**, 163–170 (2012).
23. G. Meng et al., “High-throughput synapse-resolving two-photon fluorescence microendoscopy for deep-brain volumetric imaging in vivo,” *eLife* **8**, e40805 (2019).
24. H. Dana et al., “High-performance calcium sensors for imaging activity in neuronal populations and microcompartments,” *Nat. Methods* **16**, 649–657 (2019).
25. Y. Kajikawa and C. E. Schroeder, “How local is the local field potential?” *Neuron* **72**, 847–858 (2011).
26. O. Herreras, “Local field potentials: myths and misunderstandings,” *Front. Neural Circuits* **10**, 101 (2016).
27. J. Losacco et al., “Learning improves decoding of odor identity with phase-referenced oscillations in the olfactory bulb,” *eLife* **9**, e52583 (2020).
28. D. Curran-Everett, “Multiple comparisons: philosophies and illustrations,” *Am. J. Physiol. – Regul. Integr. Comp. Physiol.* **279**, R1–R8 (2000).
29. M. S. Jog et al., “Tetrode technology: advances in implantable hardware, neuroimaging, and data analysis techniques,” *J. Neurosci. Methods* **117**, 141–152 (2002).
30. A. Li, D. H. Gire, and D. Y. Restrepo, “Spike-field coherence in a population of olfactory bulb neurons differentiates between odors irrespective of associated outcome,” *J. Neurosci.* **35**, 5808–5822 (2015).
31. K. J. Friston et al., “LFP and oscillations-what do they tell us?” *Curr. Opin. Neurobiol.* **31**, 1–6 (2015).
32. J. L. Swanson et al., “Advancements in the quest to map, monitor, and manipulate neural circuitry,” *Front. Neural Circuits* **16**, 886302 (2022).
33. W. Zong et al., “Large-scale two-photon calcium imaging in freely moving mice,” *Cell* **185**, 1240–1256.e30 (2022).
34. C. H. Yu et al., “Diesel2p mesoscope with dual independent scan engines for flexible capture of dynamics in distributed neural circuitry,” *Nat. Commun.* **12**, 6639 (2021).
35. F. Helmchen and W. Denk, “Deep tissue two-photon microscopy,” *Nat. Methods* **2**, 932–940 (2005).
36. N. J. Sofroniew et al., “A large field of view two-photon mesoscope with subcellular resolution for in vivo imaging,” *eLife* **5**, e14472 (2016).
37. G. Barbera et al., “A wireless miniScope for deep brain imaging in freely moving mice,” *J. Neurosci. Methods* **323**, 56–60 (2019).
38. J. H. Siegle and M. A. Wilson, “Enhancement of encoding and retrieval functions through theta phase-specific manipulation of hippocampus,” *Elife* **3**, e03061 (2014).
39. V. Kanta, D. Pare, and D. B. Headley, “Closed-loop control of gamma oscillations in the amygdala demonstrates their role in spatial memory consolidation,” *Nat. Commun.* **10**, 3970 (2019).
40. N. A. Steinmetz et al., “Neuropixels 2.0: a miniaturized high-density probe for stable, long-term brain recordings,” *Science* **372**, eabf4588 (2021).
41. L. Grosenick, J. H. Marshel, and K. Deisseroth, “Closed-loop and activity-guided optogenetic control,” *Neuron* **86**, 106 (2015).

**Connor M. McCullough** received his BS degree in physics from the University of Florida in 2015. Currently, he is finishing his doctoral degree in bioengineering developing methods for recording *in vivo* neural activity in the Gibson Biophotonics Laboratory at the University of Colorado, Anschutz Medical Campus.

**Daniel Ramirez-Gordillo** is an assistant professor in the neurosurgery department at the University of Colorado Anschutz Medical Campus. He received his PhD degree in biology/



neurobiology from New Mexico State University. He combines multiple approaches and techniques to study decision making as it related to learning and memory.

**Michael Hall:** Biography not available.

**Gregory L. Futia** received his PhD in bioengineering from the University of Colorado for work on rare cell detection using optical microscopy and his MS degree in electrical engineering from Colorado State University specializing in optics and developing spatial frequency modulated imaging. Currently, he is working on engineering multiphoton microscopes for *in vivo* optical neural recording and stimulation as a research associate in the Gibson Biophotonics Laboratory at the University of Colorado, Anschutz Medical Campus.

**Andrew K. Moran** is a postdoctoral fellow in the Department of Cell and Developmental Biology at the University of Colorado, Anschutz Medical Campus. He received his PhD degree in neuroscience from the University of Utah in optical dissection of neural circuits in the olfactory bulb using fluorescent glutamate sensors. His postdoctoral work encompasses investigating brain circuitry responsible for odor-driven, reach behavior.

**Emily A. Gibson** received her PhD in physics from the University of Colorado at Boulder with a specialization in nonlinear optics. Currently, he is working as an associate professor in the Department of Bioengineering, University of Colorado, Anschutz Medical Campus with a joint appointment in the Department of Physiology and Biophysics and Neuroscience Program. Her research interest includes the development of optical technologies for clinical and biomedical research applications. She has expertise in microscopy and spectroscopy techniques for measurement of biological samples from cellular to *in vivo* models.

**Diego Restrepo** received his MSc and PhD degrees in biophysics from the University of Rochester. Currently, he is working as a professor in the Department of Cell and Developmental Biology at the University of Colorado, Anschutz Medical Campus. He employs and develops new methods in advanced neurophotonics, multielectrode rerecording, and neural modulation to determine the circuit basis of olfactory decision making and studies the role of viral infection of the olfactory system in neurodegeneration.